Research Article

Porous, multi-layered piezoelectric composites based on highly oriented PZT/PVDF electrospinning fibers for high-performance piezoelectric nanogenerators

Xiangxin DU, Zheng ZHOU, Zhao ZHANG, Liqin YAO,
Qilong ZHANG[*], Hui YANG

School of Materials Science and Engineering, State Key Laboratory of Silicon Materials,
Zhejiang University, Hangzhou 310027, China

© The Author(s) 2021.

Abstract: Piezoelectric nanogenerators (PENGs) that can harvest mechanical energy from ambient environment have broad prospects for multi-functional applications. Here, multi-layered piezoelectric composites with a porous structure based on highly oriented $Pb(Zr_{0.52}Ti_{0.48})O_3$/PVDF (PZT/PVDF) electrospinning fibers are prepared via a laminating method to construct high-performance PENGs. PZT particles as piezoelectric reinforcing phases are embedded in PVDF fibers and facilitate the formation of polar β phase in PVDF. The multi-layered, porous structure effectively promotes the overall polarization and surface bound charge density, resulting in a highly efficient electromechanical conversion. The PENG based on 10 wt% PZT/PVDF composite fibers with a 220 μm film thickness outputs an optimal voltage of 62.0 V and a power of 136.9 μW, which are 3.4 and 6.5 times those of 10 wt% PZT/PVDF casting film-based PENG, respectively. Importantly, the PENG shows a high sensitivity of 12.4 $V \cdot N^{-1}$, presenting a significant advantage in comparison to PENGs with other porous structures. In addition, the composites show excellent flexibility with a Young's modulus of 227.2 MPa and an elongation of 262.3%. This study shows a great potential application of piezoelectric fiber composites in flexible energy harvesting devices.

Keywords: piezoelectric composite; piezoelectric nanogenerator (PENG); porous structure; $Pb(Zr_{0.52}Ti_{0.48})O_3$ (PZT); PZT/PVDF electrospinning fibers; flexible self-powered devices

1 Introduction

With the urgent need for multi-functional, portable, light, and wearable electronic devices, piezoelectric nanogenerators (PENGs) capable of high-efficiency energy harvesting from ambient environment are used as self-powered devices nowadays. PENG converts the stress applied on the material into electricity by means of the inherent piezoelectric effect. Piezoelectric effect refers to the phenomenon in which the material without a center of structural symmetry changes its internal polarization with external pressure, giving rise to the same amount of heterogeneous charges on the surface. At first, perovskite piezoelectric ceramics ((K,

* Corresponding author.
E-mail: mse237@zju.edu.cn

Na,Li)NbO$_3$ [1,2], BaTiO$_3$ [3], and Pb(Zr,Ti)O$_3$ [4,5]) and piezoelectric semiconductors (ZnS [6], ZnO [7], and CdS [8]) attracted lots of attention due to their excellent piezoelectric coefficients, but the brittleness of their own limited the application in flexible electric devices. On the contrary, piezoelectric polymer has good flexibility but much lower piezoelectric coefficient comparing to the piezoceramics/semiconductors. Therefore, a large number of organic/inorganic composite-based PENGs with complementary advantages of piezoelectric ceramics/semiconductors and polymers have become the focus of academic research.

To date, the familiar structure of the piezoelectric composites is to embed piezoelectric inorganic particles simply and randomly into flexible polymers [9]. This structure integrates the advantages of piezoelectric ceramics/semiconductors and polymers, but is not effectively better in the output performance of the composite-based PENGs because of particle aggregation [10] or isolation microstructure [11], as well as insufficient flexibility. Hence, some other novel structures are proposed to solve these problems. For instance, vertically aligned BaTiO$_3$ nanowire-based PENGs [12] are developed to reduce the isolation microstructure, getting an output power of 6.27 mW·cm^{-2}. A three-dimensional (3D) porous network structure [13] is reported to ensure the dispersion uniformity of piezoelectric particles in the matrix. In addition, stress transfer is also enhanced, which is further simulated by Comsol simulation [14], demonstrating an effective load transfer.

PENGs based on fibers possess the most satisfactory mechanical features such as light weight, flexiblity, and stretchiness, which makes this kind of material ideal to be applied as the interface platform among humans, environment, and machines [15,16]. Electrospinning is a mature and applicable technique for generating ultrathin fibers to be used in various fields like biomedical science, filtration, and energy harvesting [17,18]. Considering the PENGs for energy harvesting, most fiber-based PENGs are made of membranes originally from electrospinning. For example, the BCZT–0.2 mol% Y membranes are fabricated through electrospinning technology [19], and a voltage of 3 V is generated by finger tapping. (Na,K)NbO$_3$-based P(VDF–TrFE) electrospinning membranes are also reported, the corresponding open-circuit voltage reaches 12.2 V, and the highest power is 33.2 μW [20]. Additionally, Pb(Zr$_{0.52}$Ti$_{0.48}$)O$_3$/PVDF (PZT/PVDF) composite fibers combining the strengths of the excellent piezoelectricity and flexibility are studied. References [21,22] focus on the piezoelectric performance of original electrospinning membrane, whose output voltage is as small as 184 mV. References [23,24] study the ferroelectric, dielectric, and mechanical properties of the PZT/PVDF fiber film, but do not give a description of output performance. It can be concluded that the output power of the membrane directly obtained by electrospinning is still low. To be specific, in the process of electrospinning, the low conductivity of polymer fibers causes residual charges to accumulate on the surface of collected fibers [25], which hinders further fibers collecting from the similarly charged jet. As a result, the adhesion between the fibers is reduced and a pretty loose structure is formed. The largely loose structure leads to poor membrane resilience and low fiber density. Under pressure, the membrane is confronted with more overall deformation instead of fiber deformation, which limits the output power of the membrane. Besides, it is difficult for the membranes to be sandwiched directly into electrodes without destroying fiber arrangement.

In this study, several membranes were pressed together via a laminating method into a fiber film in that every individual fiber can be accessible to stress to achieve piezoelectric effect, thus improving the output performance of PENGs. We have successfully prepared the dense fiber films with contact surface fibers and separated internal fibers, where PVDF as a flexible piezoelectric substrate was dissolved to be spun into oriented fibers due to the advantages of high flexibility, good piezoelectricity, and low cost [26]. In addition, PZT particles with excellent piezoelectricity and large residual polarization were imbedded into the fibers to further enhance the piezoelectric capability. Herein, we explored the structural characteristics and the piezoelectric output performance of the PENGs based on the PZT/PVDF flexible piezoelectric fiber composite. Differing from conventional piezoelectric composites, the PZT/PVDF fiber composites from pressed membranes exhibit superior electrical properties. The 10 wt% PZT/PVDF composite fiber-based PENG (220 μm) outputs the maximum voltage of 62.0 V and the power of 136.9 μW, which are 3.4 and 6.5 times those of the control PENG (10 wt% PZT/PVDF casting film-based PENG), respectively, under a periodic pressure of 5 N. This study provides an efficient but simple way to prepare high-performance small-scale PENGs.

2 Experimental

2.1 Preparation of precursor solution

The PZT powders were prepared through high-energy ball milling method [27]. The precursor solution shown in Fig. 1 was prepared as follows: First, a certain amount of PZT powders were ultrasonically dispersed in a mixture of N,N-dimethylformamide (DMF; AR, 99.5%, Shanghai Aladdin Biochemical Technology Co., Ltd., China) and acetone (AR, 99.5% Sinopharm Chemical Reagent Co., Ltd., China), in which DMF/acetone volume ratio is 2:3. Second, 1 g PVDF (Solef 6010, M_w = 500,000–600,000 g/mol, Solvay S.A., Belgium) was gradually added into the solution. Third, the mixture was magnetically stirred at 50 ℃ for 5 h to dissolve the polymer powders completely to get a homogeneous solution.

2.2 Electrospinning deposition

During electrospinning, the temperature and relative humidity were set to 27 ℃ and 40%–60%, respectively. Then, the injected rate was set to 1.0 mL/h with a 19-gauge stainless steel needle (inner diameter = 0.72 mm), which was connected to the positive electrode of the power supply device inside electrospinning machine (TL-01, Tongli Micronano Technology Co., Ltd., China). And the negative electrode was attached to a metallic cylinder, which was covered with an Al foil as the fiber collector in a rotating speed of 3000 r/min, and the spinning sprayers moved evenly with a speed of 2.6 mm/s. A constant voltage of 11.20 kV was supplied between the positive and negative electrodes in a distance of 12 cm. Finally, the highly oriented fiber membrane was obtained under the potential difference between positive and negative electrodes. The membrane was then dried at 60 ℃ overnight to ensure that the residual solvent evaporated completely and needed no additional poling process.

2.3 Fabrication of the PZT/PVDF PENGs

The fiber films were fabricated by a laminating method as follows: cutting the fiber membrane into small pieces with the size of 2 cm × 4 cm, adding them layer by layer along the same direction, and then applying a press of 15 MPa for 1 h at 30 ℃. Finally, all the fiber layers were compressed together, and the fiber film with a certain thickness was fabricated. The nickel tape acting as electrode was fixed tightly on the either surface of the fiber film. Further, thin polyethylene terephthalate (PET) films (30 μm) were selected to package all the samples in case of pollution on the film surface when they were exposed to the lab environment. The samples with 0, 2, 4, 6, 8, and 10 wt% PZT content were respectively named as f-P 0.00, f-P 0.02, f-P 0.04, f-P 0.06, f-P 0.08, and f-P 0.10, in which f means fibers, P means PZT particles, and 0.00, 0.02, 0.04, 0.06, 0.08, 0.10 means the mass fraction of PZT particles.

2.4 Characterizations

The morphology of composite films was observed by the scanning electron microscope (SEM; SU-8010, Hitachi, Japan). A mapping test was conducted on the PVDF/PZT fibers with the energy dispersive X-ray
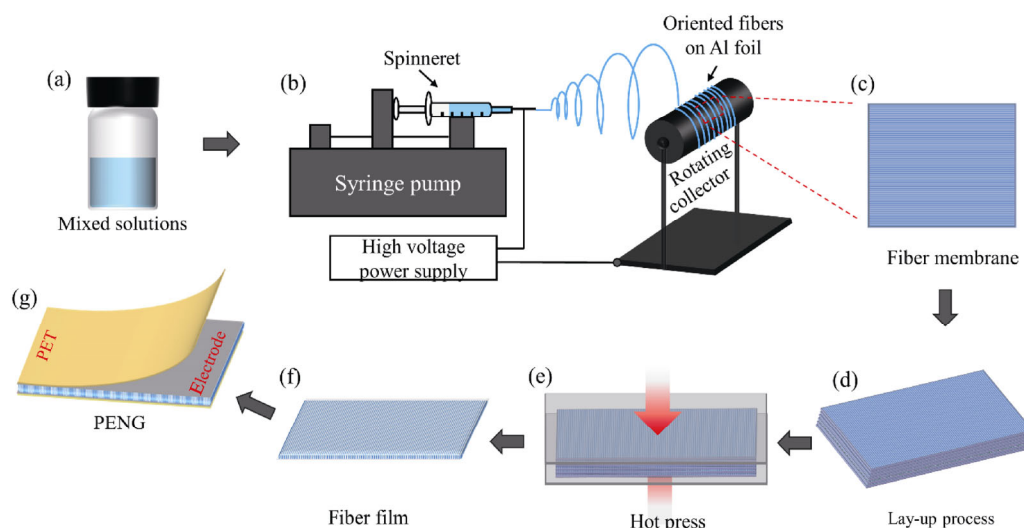

Fig. 1 Abridged general view of the PENG process routing.

spectroscopy to characterize the elements and their distribution. Phase structures of the films were analyzed by X-ray diffraction (XRD; X'Pert PRO, PANalytical, the Netherlands) with Cu Kα radiation. Besides, to explore the crystalline phase of PVDF in more detail, differential scanning calorimetry analysis (DSC; Q200, TA Instruments, USA) and a Fourier-transform infrared spectroscope (FTIR; Nicolet 5700, Thermo Fisher, USA) were used. The surface characteristics were tested by Analysis IR2 (nanoIR2-fs, Analysis Instruments, USA). The open-circuit voltages of PZT/PVDF fiber-based PENGs were collected by a digital oscilloscope (TBS2104, Tektronix, USA). The output currents were calculated based on Ohm's law: $I = U/R$ (I, U, and R represent current, voltage, and resistance, respectively) through loading external resistance. The mechanical performance of the films was analyzed at room temperature by the tension test (Zwick/Roell Z020, Germany).

3   Results and discussion

3.1   Fiber morphology and device structure

As a method for preparing nano/microscale composite fibers, electrospinning has been widely applied in the field of energy harvesting. From this study, we successfully prepared PVDF oriented fibers doped with PZT particles by adjusting the parameters of electrospinning and the viscosity of the mixed solution.

In Fig. 2(a), the PZT/PVDF fibers show a high degree of orientation. Theoretically, aligned fibers are easier to be compressed than disordered ones without the obstruction of cross fibers. Moreover, the aligned fiber membranes show higher piezoelectric output performance than the disordered fiber membranes owing to uniformly oriented direction of β phase [28]. The element mappings of Zr, Ti, Pb, and O are displayed in Figs. 2(a$_1$)–2(a$_4$), respectively, and each element is evenly distributed over the fibers regardless of the particle size. It is worth noting that the PZT particles in the experiment are irregular blocks (Fig. S1(a) in the Electronic Supplemetary Material (ESM)), which possess larger specific surface area and provide more space for the formation of polar phases than spherical PZT particles. The PZT particle size statistics and the XRD result are exhibited in Figs. S1(b) and S1(c) in the ESM. The enlarged element mapping for PZT particles in Fig. S2 in the ESM further illustrates the four elements of PZT particles, and the atom ratio approaches the ideal ratio. The fiber diameter distribution (Fig. 1(b)) in accordance with Fig. 1(a) ranges from 0.5 to 3.0 μm. Actually, when PZT content increases, the mixed solution becomes more viscous and thus the average fiber diameter becomes larger, as shown in Fig. S3 in the ESM.

Owing to the loose structure of the fiber membranes, the output signal is so weak and unstable that it is susceptible to surroundings. To solve the problem, a laminating method is used to compress several fiber
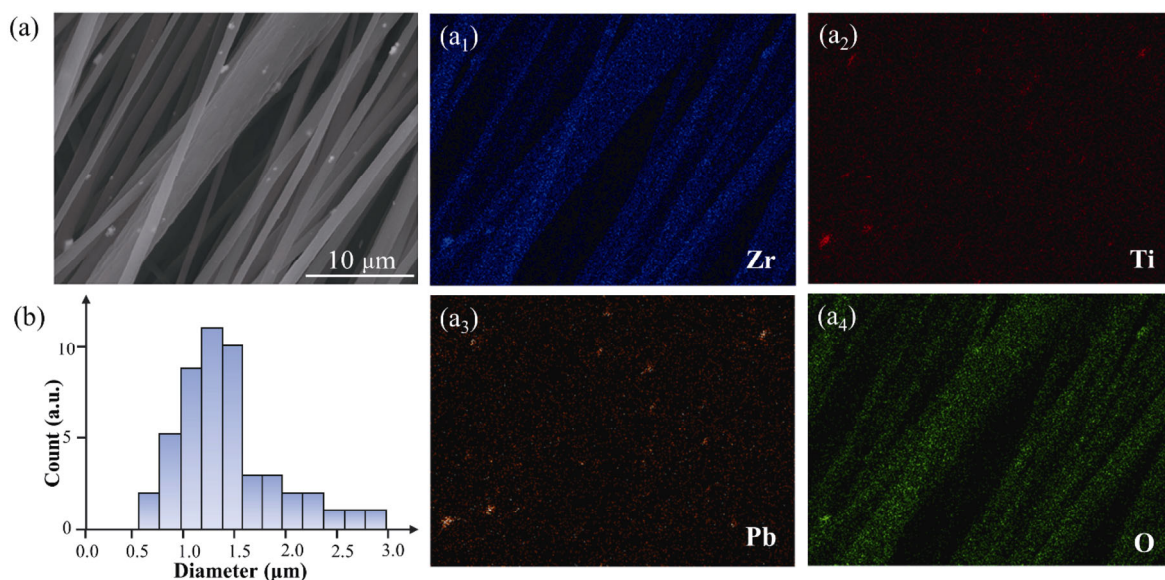

Fig. 2 (a) SEM image of 10 wt% PZT/PVDF electrospinning fibers: (a$_1$–a$_4$) the element mapping of electrospinning fibers. (b) Statistical results of the fiber diameter distribution.

membranes together [29]. It is worth noting that we conduct the process at room temperature (30 ℃) in case that fibers melt at higher temperatures. Herein, we superimposed the membranes layer by layer (2, 4, 6, 8, and 12 layers), and then compressed them under 15 MPa for 60 min. The fiber films with thicknesses of ~40, ~100, ~160, ~190, and ~220 μm were obtained. As shown in Fig. 3(a), the 220 μm film remains good flexibility. As the schematic structure shows (Fig. 3(b)), the PENG is composed of PENG packing layers, nickel tape layers, surface fibers, and layers of internal fibers. The real image of fabricated PENG with scale bar is shown in Fig. S4 in the ESM, where the left is the composite fiber membrane on aluminum foil, and the right is the PENG based on the fiber film. The effective area of the PENG depends on the counter electrodes which are 2 cm × 4 cm. The cross-section of the fiber film in Fig. 3(c) shows no obvious interface, indicating that layers of fiber membranes were well pressed together under the laminating treatment. Different from traditional laminate materials, the surface fibers (Fig. 3(d)) were squeezed together, which enhance the density of fibers on the surface. While the internal fibers still separate from each other, as Fig. 3(e) shows. This structure not only increases the bound charge density on the surface to optimize piezoelectric output, but also effectively improves the sensitivity of the composites campared with the fiber membranes. Besides, the inset in Fig. 3(e) is the zoom-in view of one single fiber and the typically pillar wrinkled surface is generally helpful to piezoelectric outputs [30].

Based on the morphology of fibers, we studied the mechanical properties of the ~220 μm f-P 0.10 film, as well as the 10 wt% PZT/PVDF cast film (220 μm). The tensile test was performed at a drawing speed of 2 mm/min, and the strain curves in Fig. 3(f) exhibit a significant difference between the cast film and the fiber film under the condition that the tensile is
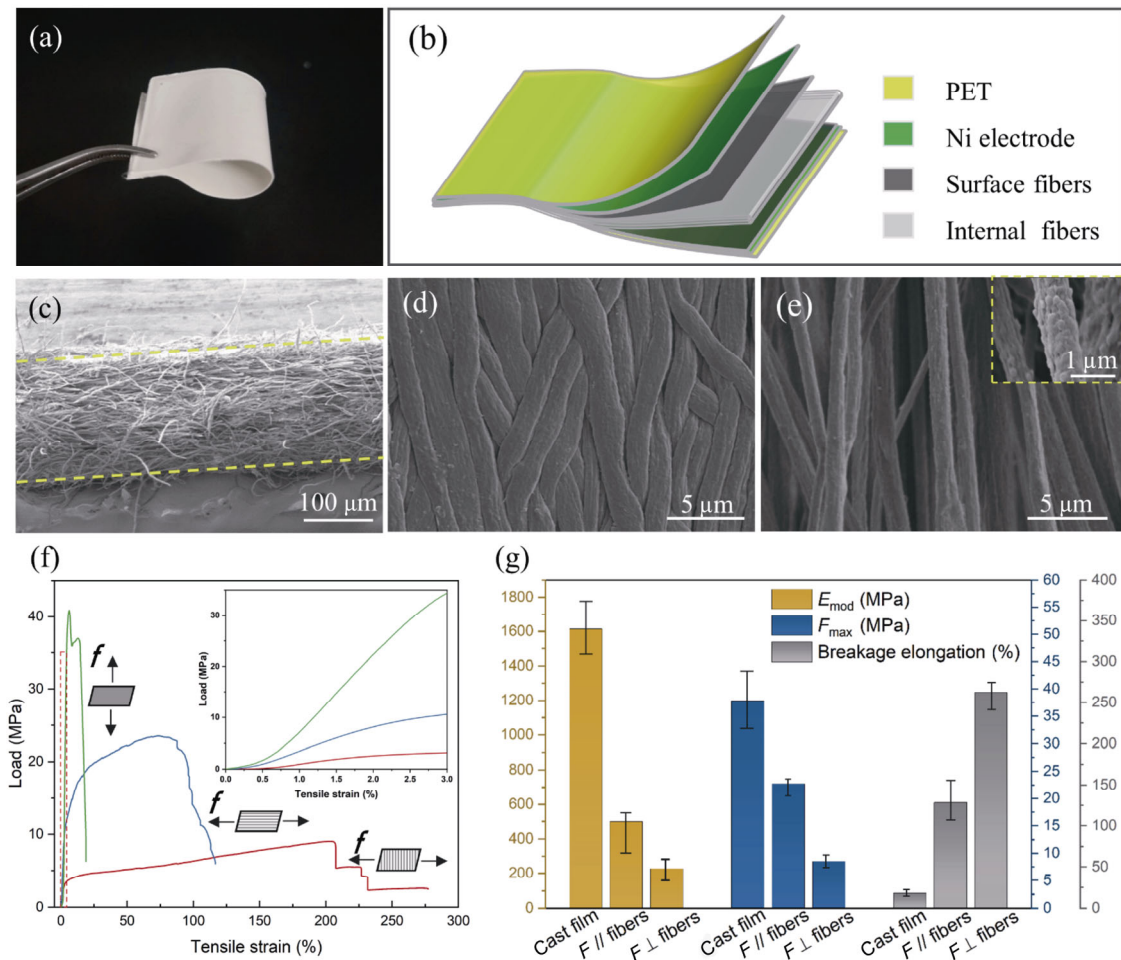

Fig. 3 (a) Photograph of the fiber film; (b) schematic structure of the PENGs; (c) SEM image of the fiber film cross section; (d) surface fibers; (e) internal fibers (the inset: the enlarged view of one single fiber); and (f) strain curves. (g) Young's modulus E_{mod}, maximum tensile strength F_{max}, and breakage elongation of 10 wt% PZT/PVDF film with a thickness of ~220 μm.

perpendicular/parallel to the axial direction of the fibers. In comparison with the cast film, the Young's modulus of fiber film dropped sharply from 1614 to 499.2 MPa (*F*//fibers) and 227.2 MPa (*F*⊥fibers), indicating that the fiber film is more flexible. The elongation at break of the fiber film increased to 262.3%, 14.8 times the breakage elongation of the cast film, which means that the fiber film has better toughness (Fig. 3(g)). Although the maximum tensile strength is reduced to 8.538 MPa, it has little impact on the fiber film, because it is mainly subjected to pressure rather than tension during application. The

decrease in Young's modulus and tensile strength may be attributed to the lower crystallinity of the fiber film, which will be mentioned in the part of crystalline characteristics. At the same time, more amorphous regions in PVDF lead to an increase in elongation at break. Table S1 in the ESM lists the average Young's modulus, maximum tensile strength, and elongation at break of f-P 0.10 film at different stretching directions and the 10 wt% PZT/PVDF cast film.

3. 2 Crystalline structure

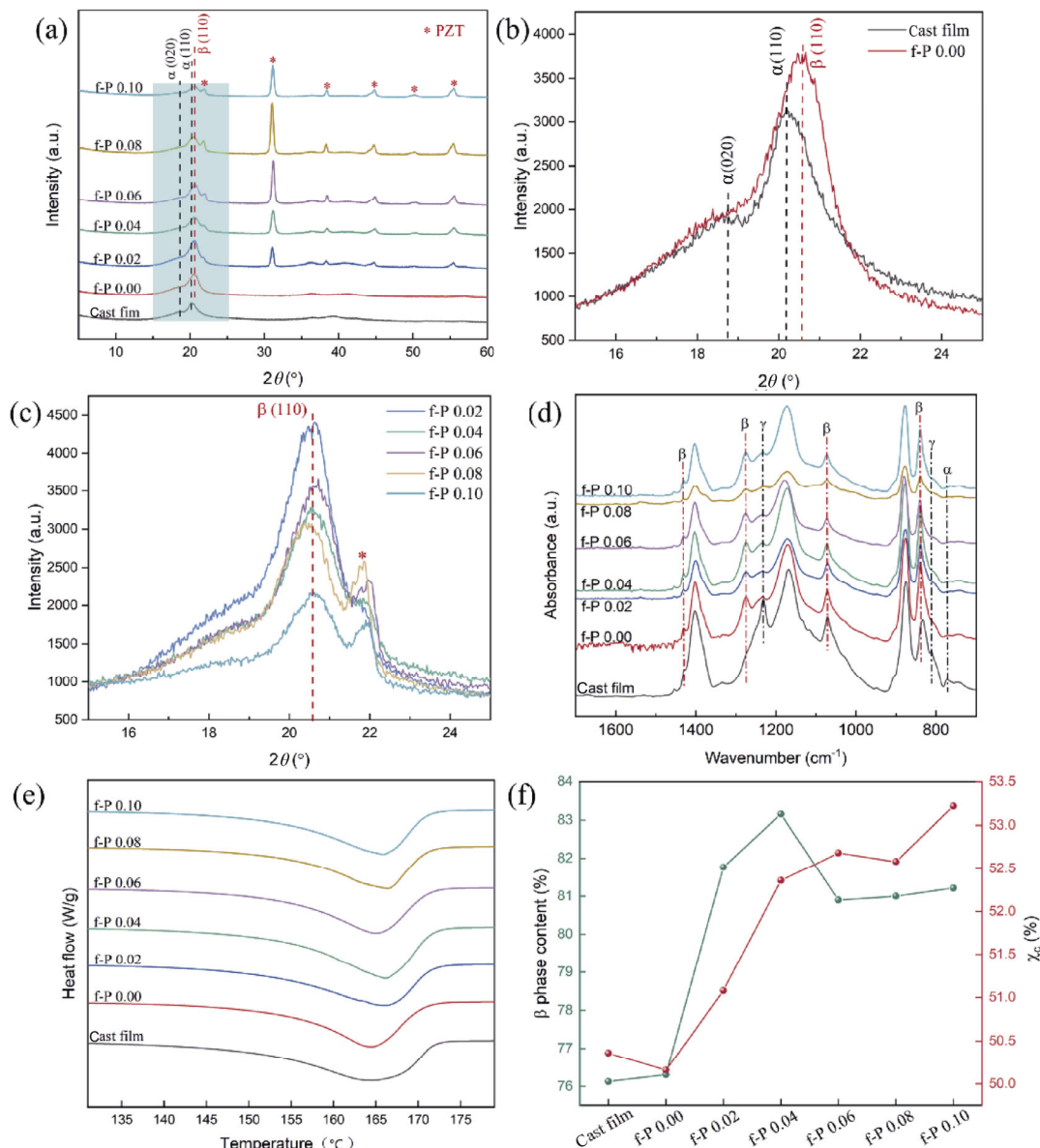In Fig. 4(a), the XRD results of the PVDF cast/fiber

Fig. 4 (a) XRD patterns, (d) FTIR spectra in ATR mode, (e) DSC curves, and (f) the calculated crystallinity degree and β phase content of pure PVDF cast film and PZT/PVDF fiber films with different PZT concentrations. Enlarged XRD view of (b) PVDF cast film and PVDF fiber film and (c) PZT/PVDF composite fiber films from 15° to 25°. χ_c represents the degree of crystallinity.

films with different PZT mass ratios exhibit the characteristic peaks of both PVDF and PZT. The typical peaks of perovskite PZT phase [31] are detected in all PZT/PVDF composite films, and the intensity gradually enhances as PZT content increases. The enlarged view of XRD patterns from 15° to 25° is illustrated in Fig. 4(b), and the pure cast film presents, prominent peaks at $2\theta =$ 18.8° and $2\theta = 20.2°$, corresponding to the (020) and (110) reflections of α phase, respectively. For fiber films, the peak at $2\theta = 18.8°$ disappears and the peak at $2\theta = 20.2°$ shifts to higher degree of $2\theta = 20.6°$, which corresponds to the (110) reflection of polar β phase. This phenomenon is attributed to high electric poling and mechanical stretching during electrospinning process. The applied electric field and stretching generally have a positive effect on the transformation of amorphous phase to polar β phase [30]. In Fig. 4(c), the curves become smoother as PZT concentration increases. For PZT particles, the excellent ferroelectricity makes them easier to be polarized by the applied electric field, and the large remnant polarization avails better piezoelectricity. PZT particles also boost the formation of β phase. Specifically, charges on the polarized PZT particle surface affect the arrangement of PVDF molecules. The interaction between the positive/negative charges on PZT surface and the electronegative –CF$_2$/ electropositive –CH$_2$ groups on PVDF facilitates alignment of PVDF chains and promotes the formation of β phase [26,32]. In addition, it is believed that mental oxides carry hydroxyl groups on their surface. The attraction between the hydroxyl groups (–OH) on PZT particles and the –CF$_2$ groups of the PVDF polymer chains results in the generation of β phase, which also supports the experimental results.

To further study the structure and crystalline characteristics of the composite fiber film, the FTIR spectra in ATR mode and DSC measurement were performed. In Fig. 4(d), the pure PVDF cast film contains several typical characteristic absorption bands. The peak at 764 cm^{-1} is designated as α phase [33]; the peaks of γ phase are located at 812 [34,35], 834 [36], and 1234 cm^{-1} [37]. The polar β phase comes from the absorption bands of 1074 and 1430 cm^{-1} [38]. For the fiber film, two new peaks corresponding to β phase appear at 840 and 1275 cm^{-1}. Besides, the β phase at 1430 cm^{-1} is enhanced, while α/γ phase reduces. The incorporation of PZT particles further suppressed the intensity of α and γ phases. Further, the observed result of FTIR spectra is consistent with the XRD data and

the amount of β phase (F_β) is calculated by Eq. (1) [39]:

$$F_\beta = \frac{I_\beta}{(K_\beta / K_\alpha) \times I_\alpha + I_\beta} \tag{1}$$

where I_α refers to the absorbance of α phase at 764 cm^{-1} in the FTIR spectra, I_β is the absorbance of β phase at 840 cm^{-1} in the FTIR spectra, and K_α and K_β are constants and represent absorption coefficients. The calculation results are shown graphically in Fig. 4(f), and the data shows that electrospinning process does enhance the percentage of β phase, but it is not as much as we expected. The f-P 0.00 film has 76.31% β phase, which is slightly higher than the cast film (76.13%). Interestingly, the addition of PZT particles significantly promoted β phase content, reaching a maximum of 83.16% in the f-P 0.04 film. When the PZT particle content further increases, the resultant high viscosity causes difficulties in the mixed solution ejecting out of the needle tip even at a higher electric field application. As a result, there is a tendency of the resultant dispersion to form higher diameter fibers with less effective orientation of the polymer chains which emphasizes the growth of α phase rather than β phase [40]. Such phenomena can also be reflected in the crystallization curves (Fig. 4(e)), and the overall crystallization was calculated using Eq. (2):

$$\chi_c = \frac{\Delta H_f}{(1 - \phi) \times \Delta H_m^{100}} \tag{2}$$

where ΔH_f is the melting enthalpy of PVDF/PZT composites, ϕ is the mass ratio of PZT particles in PVDF/PZT composite, and ΔH_m^{100} represents the melting enthalpy of a 100% crystalline PVDF ($\Delta H_m^{100} =$ 104.7 J/g). In Fig. 4(f), the crystallinity of the f-P 0.00 film is 50.16%, slightly lower than that of the cast film (50.35%). Too many interfaces between the fibers reduce the chances of crystallization. PZT particles significantly improve the crystallinity of the fiber film, which owes to the increase of β phase when PZT content is 2%–4% and the formation of α phase when the PZT content is 6%–10%, because the higher diameter fibers with less effective polymer chains stretching favor the generation of α phase.

3. 3 Surface characteristics

Essentially, the piezoelectric performance depends on the polarization intensity brought about by the internal crystal structure, and also depends on the bound charge density of the film surface. Here, we studied the

characteristics of the internal/surface fibers of f-P 0.10 film (220 μm) and 10 wt% PZT/PVDF cast film (220 μm) for comparison. First, the topographic maps are shown in Figs. 5(a)–5(c). The surface of the cast film is flat, which is concluded from the almost indistinguishable overall color in Fig. 5(a). Internal fibers in Fig. 5(b) show rougher surfaces with a wider range of colors than surface fibers in Fig. 5(c), verifying that the laminating process improves the density and flatness of the surface fibers without destroying the porous fibrous structure. Second, the surface potential positively correlated with the surface charge density is shown in Figs. 5(d) and 5(f). In contrast to the cast film, both surface fibers and internal fibers exhibit stronger potentials with the color shifting to red or blue. Whether it is positive or negative rests with the testing surface as overall polarization intensity is parallel to the thickness direction and directional. This is a pretty good proof that multi-layered porous fiber film has more surface charges than the cast film. Third, the surface phases are also discussed in Figs. 5(g)–5(i). To ensure that the color distinction shown in two-dimensional (2D) image is attributed to the reflection of different phases, not the surface height gap, the 3D images have also been displayed in Figs. 5(j)–5(l). Obviously, 2D and 3D do not share the same pattern.

Despite it is impossible to distinguish each specific color corresponding to a specific phase, there is a striking contrast between the fiber film and cast film, especially in 3D images. The surface phase image of the cast film shown in Fig. 5(j) looks like green grass, and shows greater stiffness in accordance with the results of the tensile test, which proves greater crystallinity. It may be mainly composed of nonpolar α phase and amorphous polymer. While the surface phase images of fibers in Figs. 5(k) and 5(l) look more like a yellow forest, where more polar β phases, less α phases, and more amorphous polymers exist. The orange regions indicate the gaps between the fibers or the holes on fibers. It is worth mentioning that there is almost no difference in surface potential and phases between surface and internal fibers, suggesting that mechanical compression makes no difference to the crystalline structure of the PZT/PVDF composite fibers [41].

3.4 Piezoelectric properties

Figure 6(a) illustrates a piezoelectric model of the PZT/PVDF fiber-based PENGs. Here, the –CH$_2$–CF$_2$– chains in PVDF and the polarized ferroelectric domains in PZT particles are regarded as dipoles, as shown in
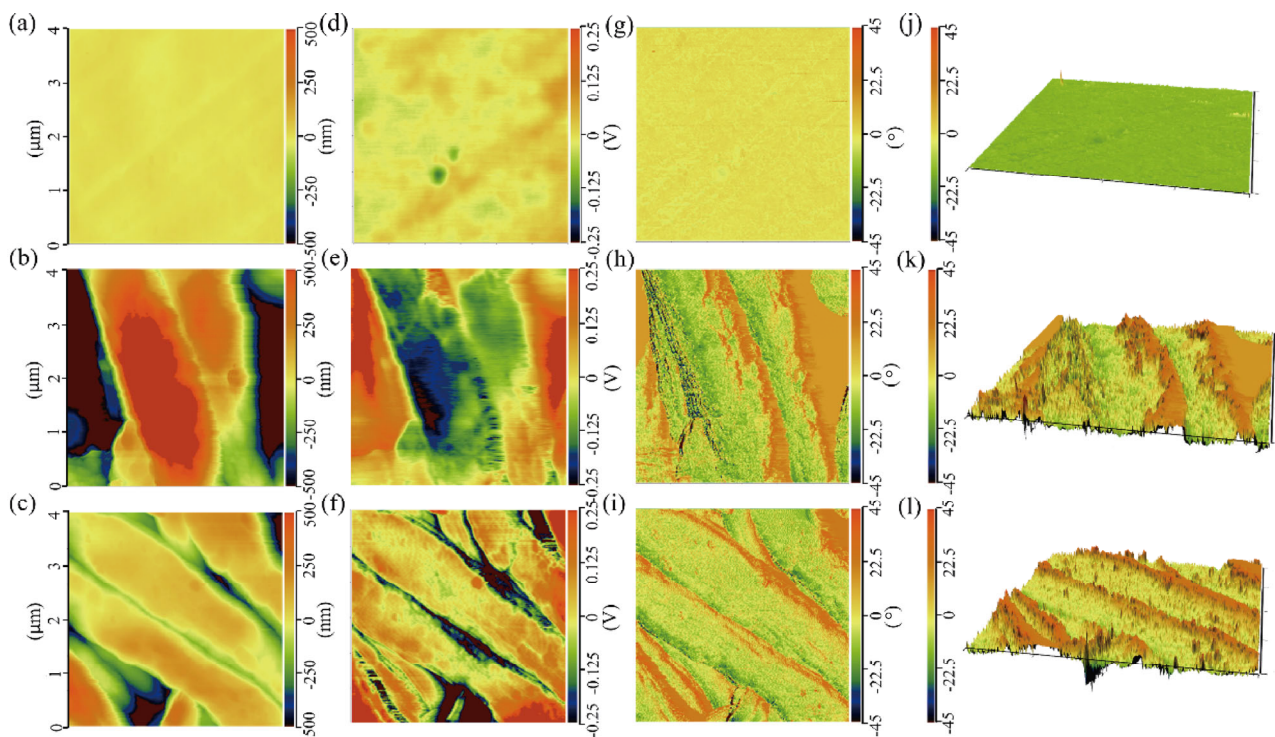

Fig. 5 Topographic images of (a) cast film, (b) internal fibers, (c) surface fibers; KPFM images of (d) cast film, (e) internal fibers, (f) surface fibers; phase images of (g, j) cast film, (h, k) internal fibers, and (i, l) surface fibers in 10 wt% PZT/PVDF PENGs.
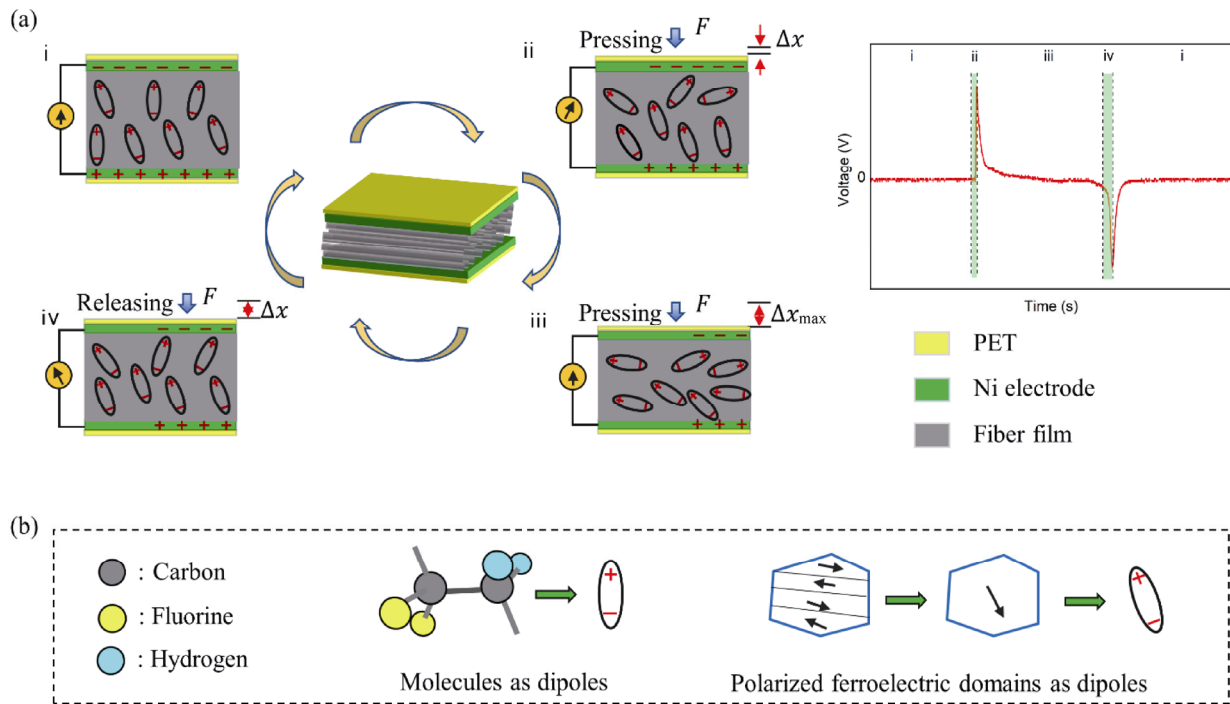
Fig. 6 (a) Schematic diagram of the mechanism for the piezoelectric performance of PZT/PVDF fiber-based PENGs and (b) abstract diagram of the dipoles about PVDF molecules and PZT ferroelectric domains inside the fibers.

Fig. 6(b). All the dipoles align in the same direction normal to the fiber axis. Under the high-potential electric field in the electrospinning process, most of the dipoles rotate to the same direction, generating an internal electric potential. To balance the potential, external electrons are bound to the surface. When external pressure is applied, the PENG is compressed by Δx and the dipoles rotate, reducing the internal dipolar momentum along the film thickness. At the same time, the bound electrons on the surface show an opposing potential and the film exhibits polarity as a whole. As Δx becomes longer, the overall polarization increases, followed by an increase in output voltage (the inset (ii) in Fig. 6(a)). The free electrons in electrodes gradually flow to the high-potential side through external circuit to offset the potential difference. When the compression deformation reaches Δx_{max}, the film reaches a new balance and shows no polarity. At this time, the output voltage drops to zero. Subsequently, when the external pressure is released, dipoles rotate to the original state gradually, thereby generating a reverse output voltage and the free electrons flow back to the original side.

Considering that the frequency of driving pressure from human motion (walking, running, joint motion, etc.) is relatively low, the output voltage signals were collected at a frequency of 3 Hz under a periodic pressure of 5 N. Since PZT has a large piezoelectric constant, it is speculated that PZT particles play a predominant role in the piezoelectric performance of the composite [28,36]. The more incorporation of PZT particles is, the better electrical output performance of the PENGs is. However, when PZT content exceeds 10 wt%, the consequent viscosity increase creates difficulties in the ejection of the composite solution out of the needle tip. Therefore, we first explored the output voltage of f-P 0.10 fiber-based PENGs with thicknesses of ~40, ~100, ~160, ~190, and ~220 μm. As shown in Fig. 7(a), all signals are very stable, and the voltage peak tends to rise as the film thickness increases. The laminating process increases dipolar momentum and overall polarization inside the film, as well as stress transfer, followed by the improvement of piezoelectric conversion capacity. In addition, it is expected that the capacity can be further enhanced by increasing thickness. For example, when the thickness is 500 μm, the output voltage can reach as high as 92 V (Fig. S7 in the ESM). Second, at the same thickness of ~220 μm, we studied the output voltage of the fiber-based PENGs with the PZT contents of 0, 2, 4, 6, 8, and 10 wt%. In Fig. 7(b), the output voltage is positively correlated with the content of PZT particles,
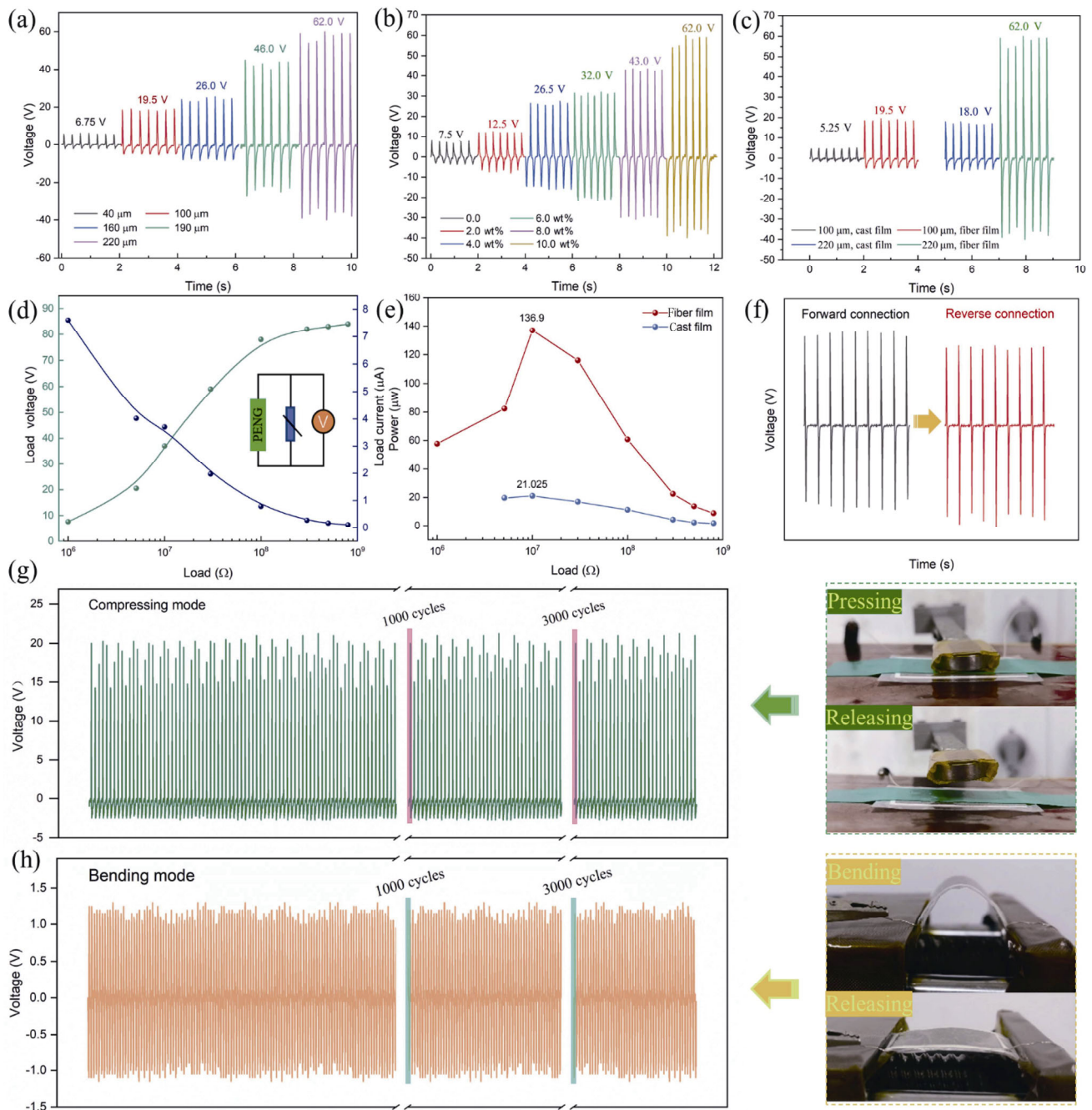
Fig. 7 (a) Output voltages of f-P 0.10 fiber-based PENGs with different film thicknesses; (b) output voltages of fiber-based PENGs with various PZT contents (~220 μm); (c) output voltage contrasts between the f-P 0.10 fiber-based PENGs and 10 wt% PZT/PVDF cast film-based PENGs; (d) output voltages and calculated currents; (e) output powers of the f-P 0.10 fiber-based PENG with a film thickness of 220 μm under various external resistance loads; (f) output voltages of f-P 0.10 fiber-based PENG in a condition of reversing electrodes; (g) cyclic output voltages of the f-P 0.10 fiber-based PENG (220 μm) under the compressing mode with ~1.0 N pressure at a frequency of 10 Hz; (h) cyclic output voltages of the f-P 0.10 fiber-based PENG (220 μm) under bending mode at a frequency of 3 Hz.

and reaches the maximum of 62.0 V in the sample f-P 0.10 fiber-based PENG. It is about 8.3 times the output voltage of the f-P 0.00 fiber-based PENG (7.5 V), because PZT particles not only possess strong piezoelectricity, but also promote polar β phase generating in PVDF. Accordingly, the short-circuit currents show the same trend as PZT particles or film thickness increase (Fig. S5 in the ESM) and so are load

currents (Fig. S6 in the ESM). To prove the superiority of the fiber-based PENGs, cast film-based PENGs with the same film thickness were prepared as a comparison. In Fig. 7(c), the f-P 0.10 fiber-based PENGs output voltages which are 3.7 times (100 μm) and 3.4 times (220 μm) the voltages of the 10 wt% PZT/PVDF cast film-based PENGs, respectively. Further, The PENG with a film thickness of 220 μm was connected to different load resistances ranging from 1 to 800 MΩ (Fig. 7(d)). As the inset in Fig. 7(d) shows, the generator acts as a power source, which connects in series with load resistance, and the oscilloscope as voltmeter is connected in parallel with load resistance. As the load resistance increases to 500 MΩ, the load voltage gradually rises to a constant value of ~83 V, whereas the load current gradually decreases from 7.6 to 0.105 μA. Correspondingly, the maximum output power is 136.9 μW at the load resistance of 10 MΩ, which is 6.5 times the power of the 220 μm thick cast film-based PENG (21.025 μW) (Fig. 7(e)).

For verifying the piezoelectric signal, a switching polarity test was carried out [37,42]. As Fig. 7(f) shows, the output voltage reverses as the circuit connection reverses, confirming that the signals are authentic piezoelectric outputs. The output performance stability was also tested under compressing and bending modes. As seen in Figs. 7(g) and 7(h), the output voltage of the f-P 0.10 fiber-based PENG is stable after 3000 cycles. Benefitting from the multi-layered porous structure, the f-P 0.10 fiber-based PENG (220 μm) shows high sensitivity to pressure. Under the pressure of ~2 N, its output voltage reaches ~20 V. Sensitivity (S) is also a parameter for evaluating piezoelectric output performance, and it can be calculated by [43]:

$$S = \frac{U}{F} \tag{3}$$

where U is the output voltage and F represents the applied pressure. The calculated sensitivity of the fiber-based PENG is 12.4 V·N^{-1}, which is 3.4 times the sensitivity of the cast film-based PENG (3.6 V·N^{-1}). First, the fibers through electrospinning prevent particle aggregation or isolation microstructure between particles and polymers, which hinder stress transfer in cast film-based PENGs. Second, laminating process significantly increases the possibilities of every single fiber being stressed by reducing the porosity of the fiber film. It is superior to most reported PENGs with porous structure, and the comparison is listed in Table 1.

Further application potential of the f-P 0.10 fiber-based PENG (220 μm) has been investigated, in which a rectifier bridge is used to convert AC to DC output (Fig. 8(a)). Figure 8(b) shows the rectified voltage signal of ~58 V, which directly lights up 21 LED lights in series. We also charged the capacitors with the capacitances of 1, 3.3, 10, 22, and 47 μF. As shown in Fig. 8(c), the capacitor (1 μF) voltage rapidly increases to 6.4 V within 65 s and remains stable, which means that the charging voltage tends to be a constant value at 6.4 V. The others are charged to 3.53, 1.03, 0.82, and 0.20 V, respectively. Besides, the curves increase proportionally, showing further potential for reaching the maximum charging voltage. Further, to simulate the applied scenarios, some simple human actions were applied in energy harvesting, such as finger pressing, fist beating, one side bending, and pressing on the arm. As Figs. 8(e)–8(h) show, the corresponding output voltages reach ~20, ~30, ~18, and ~4 V, respectively, clarifying that the PENGs are the promising devices to harvest mechanical energy from human motions.

Table 1   Comparison of output performance with different porous structures

| Piezoelectric filler	Matrix	Structure	U (V)	F (N)	S (V·N^{-1})	Ref.
BT NP	PVDF	Oriented	150	100	1.5	[44]
BCZTY NW	PDMS	Electrospun-oriented	3	Finger-taping	—	[21]
BT NP	PDMS	Porous-interconnected	15.5	32	0.48	[14]
BFO NP	PDMS	3D interconnected	16	35	0.46	[12]
Sm–PMN–PT NP	PDMS	Porous-interconnected	60	35	1.71	[10]
PZT NP	PDMS	Gradient-porous	152	100	1.52	[43]
PZT P	PVDF	Electrospun-oriented	62	5	12.4	This work
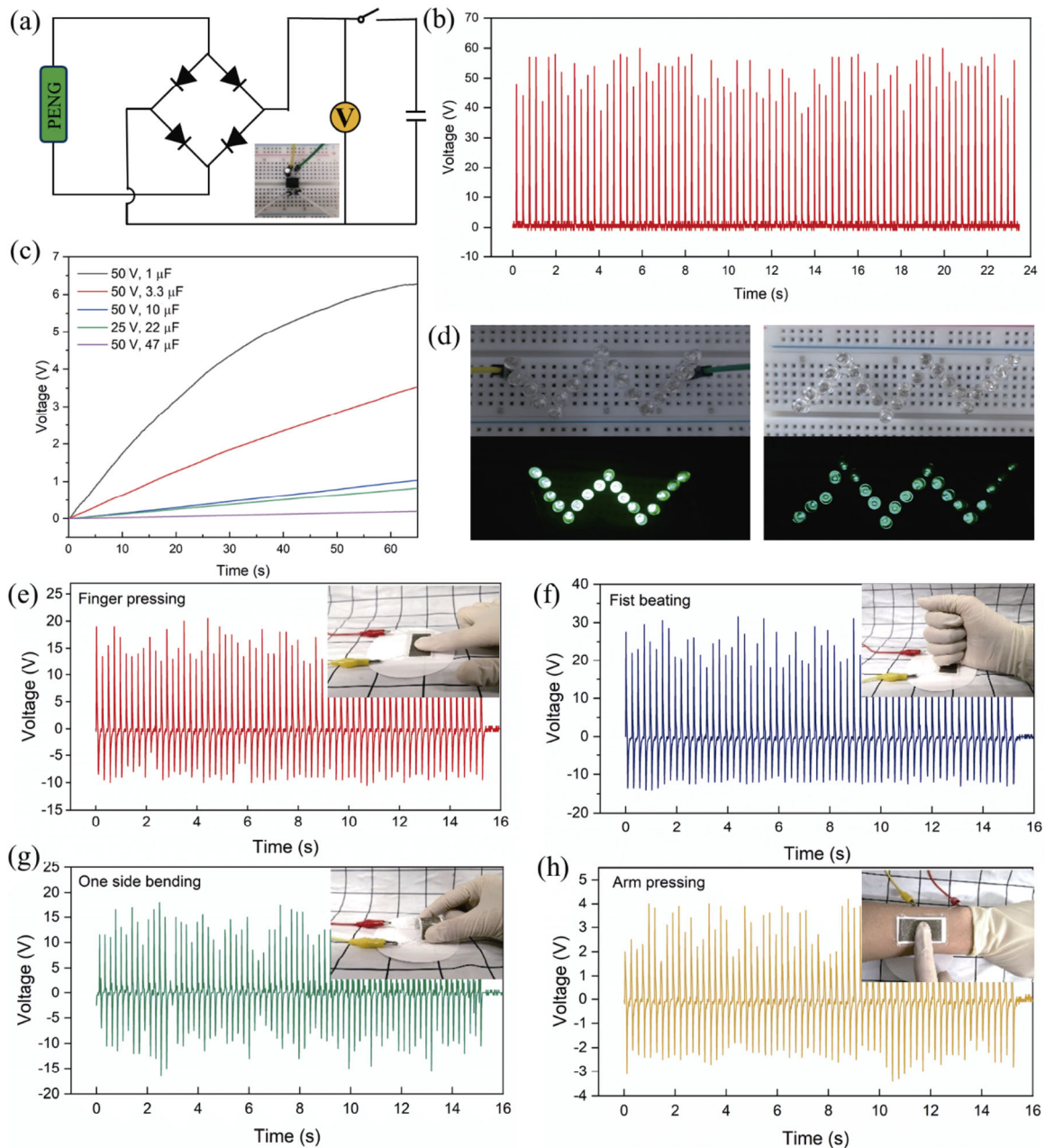
Fig. 8 (a) Equivalent circuit diagram of the charging commercial capacitor with a charging system inset; (b) rectified voltages of f-P 0.10 fiber-based PENG with a thickness of ~220 μm; (c) charging voltages of various capacitors; (d) green LEDs lit by the rectified voltages of the PENG, output voltages from f-P 0.00 fiber-based PENG under (e) finger pressing, (f) fist beating, (g) one side bending, and (h) pressing on the arm.

4 Conclusions

Porous, multi-layered PZT/PVDF piezoelectric fiber composites composed of contact surface fibers and separated internal fibers were fabricated by the laminating process. PENGs based on the porous fibrous PZT/PVDF composites with various thicknesses and PZT contents for harvesting mechanical energy have also been developed. The laminated fiber film not only has

a strong internal polarization to achieve excellent piezoelectric output, but also possesses effective stress transfer to ensure piezoelectric sensitivity. Therefore, the PENG based on the 10 wt% PZT/PVDF fiber film (~220 μm) outputs the maximum power of 136.9 μW, almost 6.5 times the power of the 10 wt% PZT/PVDF cast film-based PENG (21.025 μW). Its sensitivity is 12.4 $V \cdot N^{-1}$, which is superior to most reported PENGs with porous structures, such as 1.52 $V \cdot N^{-1}$ for gradient-

porous structure [43], 1.71 V·N^{-1} for porous interconnected structure [10], and 0.46 V·N^{-1} for 3D interconnected structure [12]. Further, the PENG based on the 10 wt% PZT/PVDF fiber film (~220 μm) was applied in capacitor charging and LED lighting, in which the capacitor (1 μF) was charged rapidly to 6.4 V within 65 s and 21 commercial green LEDs were driven to illuminate directly. The porous, multi-layered PZT/ PVDF composite fiber film presents an effective advancement in sensors, energy harvesting, and low-power electric devices with the requirement of self-powered characteristics.

Acknowledgements

Electronic Supplementary Material

Supplementary material is available in the online version of this article at https://doi.org/10.1007/s40145-021-0537-3.

References

[1] Huan Y, Zhang X, Song J, *et al*. High-performance piezoelectric composite nanogenerator based on Ag/ (K,Na)NbO$_3$ heterostructure. *Nano Energy* 2018, **50**: 62–69.

[2] Zhang MH, Hu C, Zhou Z, *et al*. Determination of polarization states in (K,Na)NbO$_3$ lead-free piezoelectric crystal. *J Adv Ceram* 2020, **9**: 204–209.

[3] Shi K, Sun B, Huang X, *et al*. Synergistic effect of graphene nanosheet and BaTiO$_3$ nanoparticles on performance enhancement of electrospun PVDF nanofiber mat for flexible piezoelectric nanogenerators. *Nano Energy* 2018, **52**: 153–162.

[4] Okayasu M, Ogawa T. Effects of loading contact on electric-power generation of lead zirconate titanate piezoelectric ceramic plate. *J Adv Ceram* 2019, **8**: 509–518.

[5] Bobić JD, Teixeira GF, Grigalaitis R, *et al*. PZT–NZF/CF ferrite flexible thick films: Structural, dielectric, ferroelectric, and magnetic characterization. *J Adv Ceram* 2019, **8**: 545–554.

[6] Lu MY, Song J, Lu MP, *et al*. ZnO−ZnS heterojunction and ZnS nanowire arrays for electricity generation. *ACS Nano* 2009, **3**: 357–362.

[7] Wang Z L, Song J. Piezoelectric nanogenerators based on zinc oxide nanowire arrays. *Science* 2006, **312**: 242–246.

[8] Lin YF, Song J, Ding Y, *et al*. Alternating the output of a CdS nanowire nanogenerator by a white-light-stimulated optoelectronic effect. *Adv Mater* 2008, **20**: 3127–3130.

[9] Zhang Y, Jeong CK, Wang J, *et al*. Flexible energy harvesting polymer composites based on biofibril-templated 3-dimensional interconnected piezoceramics. *Nano Energy* 2018, **50**: 35–42.

[10] Zhang C, Fan Y, Li H, *et al*. Fully rollable lead-free poly (vinylidene fluoride)–niobate-based nanogenerator with ultra-flexible nano-network electrodes. *ACS Nano* 2018, **12**: 4803–4811.

[11] Zhang Y, Wu M, Zhu Q, *et al*. Performance enhancement of flexible piezoelectric nanogenerator via doping and rational 3D structure design for self-powered mechanosensational system. *Adv Funct Mater* 2019, **29**: 1904259.

[12] Koka A, Sodano HA. High-sensitivity accelerometer composed of ultra-long vertically aligned Barium titanate nanowire arrays. *Nat Commun* 2013, **4**: 2682.

[13] Shi K, Huang X, Sun B, *et al*. Cellulose/BaTiO$_3$ aerogel paper based flexible piezoelectric nanogenerators and the electric coupling with triboelectricity. *Nano Energy* 2019, **57**: 450–458.

[14] Zhang G, Zhao P, Zhang X, *et al*. Flexible three-dimensional interconnected piezoelectric ceramic foam based composites for highly efficient concurrent mechanical and thermal energy harvesting. *Energy Environ Sci* 2018, **11**: 2046–2056.

[15] Dong K, Peng X, Wang ZL. Fiber/fabric-based piezoelectric and triboelectric nanogenerators for flexible/stretchable and wearable electronics and artificial intelligence. *Adv Mater* 2020, **32**: 1902549.

[16] Xie M, Hisano K, Zhu M, *et al*. Flexible multifunctional sensors for wearable and robotic applications. *Adv Mater Technol* 2019, **4**: 1800626.

[17] Xue J, Wu T, Dai Y, *et al*. Electrospinning and electrospun nanofibers: Methods, materials, and applications. *Chem Rev* 2019, **119**: 5298–5415.

[18] Cozza ES, Monticelli O, Marsano E, *et al*. On the electrospinning of PVDF: Influence of the experimental conditions on the nanofiber properties. *Polym Int* 2013, **62**: 41–48.

[19] Wu YH, Ma F, Qu JK, *et al*. Vertically-aligned lead-free BCTZY nanofibers with enhanced electrical properties for flexible piezoelectric nanogenerators. *Appl Surf Sci* 2019, **469**: 283–291.

[20] Kim SR, Yoo JH, Kim JH, *et al*. Mechanical and piezoelectric properties of surface modified (Na,K)NbO$_3$-based nanoparticle-embedded piezoelectric polymer composite nanofibers for flexible piezoelectric nanogenerators. *Nano Energy* 2021, **79**: 105445.

[21] Chamankar N, Khajavi R, Yousefi A, *et al*. A flexible piezoelectric pressure sensor based on PVDF nanocomposite fibers doped with PZT particles for energy harvesting applications. *Ceram Int* 2020, **46**: 19669–19681.

[22] Chamankar N, Khajavi R, Yousefi AA, *et al*. An experimental model for predicting the piezo and dielectric constant of PVDF–PZT nanocomposite fibers with 0–3 and 1–3 connectivity. *Ceram Int* 2020, **46**: 23567–23581.

[23] Chang J, Shen Y, Chu XC, *et al*. Large d_{33} and enhanced ferroelectric/dielectric properties of poly(vinylidene fluoride)-based composites filled with $Pb(Zr_{0.52}Ti_{0.48})O_3$ nanofibers. *RSC Adv* 2015, **5**: 51302–51307.

[24] Yun JS, Park CK, Jeong YH, *et al*. The fabrication and characterization of piezoelectric PZT/PVDF electrospun nanofiber composites. *Nanomater Nanotechnol* 2016, **6**: 20.

[25] Collins G, Federici J, Imura Y, *et al*. Charge generation, charge transport, and residual charge in the electrospinning of polymers: A review of issues and complications. *J Appl Phys* 2012, **111**: 044701.

[26] Holmes-Siedle AG, Wilson PD, Verrall AP. PVDF: An electronically-active polymer for industry. *Mater Des* 1983, **4**: 910–918.

[27] Kong LB, Zhu W, Tan OK. Preparation and characterization of $Pb(Zr_{0.52}Ti_{0.48})O_3$ ceramics from high-energy ball milling powders. *Mater Lett* 2000, **42**: 232–239.

[28] Zaarour B, Zhu L, Huang C, *et al*. Enhanced piezoelectric properties of randomly oriented and aligned electrospun PVDF fibers by regulating the surface morphology. *J Appl Polym Sci* 2019, **136**: 47049.

[29] Liao Y, Wang R, Tian M, *et al*. Fabrication of polyvinylidene fluoride (PVDF) nanofiber membranes by electro-spinning for direct contact membrane distillation. *J Membr Sci* 2013, **425–426**: 30–39.

[30] Chinaglia DL, Gregório R Jr, Vollet DR. Structural modifications in stretch-induced crystallization in PVDF films as measured by small-angle X-ray scattering. *J Appl Polym Sci* 2012, **125**: 527–535.

[31] Kwok CK, Desu SB. Low temperature perovskite formation of lead zirconate titanate thin films by a seeding process. *J Mater Res* 1993, **8**: 339–344.

[32] Araújo MC, Costa CM, Lanceros-Méndez S. Evaluation of dielectric models for ceramic/polymer composites: Effect of filler size and concentration. *J Non-Cryst Solids* 2014, **387**: 6–15.

[33] Salimi A, Yousefi AA. FTIR studies of β-phase crystal formation in stretched PVDF films. *Polym Test* 2003, **22**: 699–704.

[34] Gregorio R, Capitão RC. Morphology and phase transition of high melt temperature crystallized poly(vinylidene fluoride). *J Mater Sci* 2000, **35**: 299–306.

[35] Boccaccio T, Bottino A, Capannelli G, *et al*. Characterization of PVDF membranes by vibrational spectroscopy. *J Membr Sci* 2002, **210**: 315–329.

[36] Guo D, Chen XS, Chu XC, *et al*. *In situ* observation of the nanocrystal growth and their piezoelectric performance change in P(VDF–TrFE) films by hot stage piezoresponse force microscopy. *J Appl Phys* 2013, **113**: 187210.

[37] He S, Dong W, Guo Y, *et al*. Piezoelectric thin film on glass fiber fabric with structural hierarchy: An approach to high-performance, superflexible, cost-effective, and large-scale nanogenerators. *Nano Energy* 2019, **59**: 745–753.

[38] Yu H, Huang T, Lu M, *et al*. Enhanced power output of an electrospun PVDF/MWCNTs-based nanogenerator by tuning its conductivity. *Nanotechnology* 2013, **24**: 405401.

[39] Cai X, Lei T, Sun D, *et al*. A critical analysis of the α, β and γ phases in poly(vinylidene fluoride) using FTIR. *RSC Adv* 2017, **7**: 15382–15389.

[40] Bairagi S, Ali SW. Investigating the role of carbon nanotubes (CNTs) in the piezoelectric performance of a PVDF/KNN-based electrospun nanogenerator. *Soft Matter* 2020, **16**: 4876–4886.

[41] Chen N, Hong L. Surface phase morphology and composition of the casting films of PVDF–PVP blend. *Polymer* 2002, **43**: 1429–1436.

[42] Zhou Z, Zhang Z, Zhang Q, *et al*. Controllable core–shell $BaTiO_3$@carbon nanoparticle-enabled P(VDF–TrFE) composites: A cost-effective approach to high-performance piezoelectric nanogenerators. *ACS Appl Mater Interfaces* 2020, **12**: 1567–1576.

[43] Liu H, Lin XJ, Zhang S, *et al*. Enhanced performance of piezoelectric composite nanogenerator based on gradient porous PZT ceramic structure for energy harvesting. *J Mater Chem A* 2020, **8**: 19631–19640.

[44] Zhao Y, Liao Q, Zhang G, *et al*. High output piezoelectric nanocomposite generators composed of oriented $BaTiO_3$ NPs@PVDF. *Nano Energy* 2015, **11**: 719–727.